RESEARCH ARTICLE | JANUARY 05 2026

Self-formed core–shell InGaN nanowires: A dual-functional platform for persistent photoconductivity and self-driven photodetection

Junyong Li ; Rongli Deng ; Haibin Lin ; Xuan Pu; Richard Nötzel

AIP Advances 16, 015106 (2026)
https://doi.org/10.1063/5.0315285

Self-formed core–shell InGaN nanowires: A dual-functional platform for persistent photoconductivity and self-driven photodetection

Cite as: AIP Advances 16, 015106 (2026); doi: 10.1063/5.0315285
Submitted: 4 December 2025 • Accepted: 15 December 2025 •
Published Online: 5 January 2026

Junyong Li,[1] Rongli Deng,[1] Haibin Lin,[1] Xuan Pu,[1] and Richard Nötzel[1,2,a)]

AFFILIATIONS

[1] Guangdong Provincial Key Laboratory of Optical Information Materials and Technology, South China Academy of Advanced Optoelectronics, South China Normal University, Guangzhou 510006, People's Republic of China
[2] National Center for International Research on Green Optoelectronics, South China Normal University, Guangzhou 510006, People's Republic of China

[a)] **Author to whom correspondence should be addressed:** richard.noetzel@scnu.edu.cn.
Present address: Dipartimento di Scienza dei Materiali, Universitá di Milano-Bicocca, Via Cozzi 55, 20125 Milan, Italy

ABSTRACT

We report self-formed core–shell InGaN nanowires (NWs) grown by plasma-assisted molecular beam epitaxy on p-Si (111) substrates, which exhibit dual functionalities: persistent photoconductivity (PPC) and self-driven photodetection at 0 bias. The core–shell structure (In-rich core: 55% In, 2.05 eV; In-poor shell: 12% In, 2.76 eV) is optimized by a SiN_x passivation layer, which suppresses surface defects, stabilizes the NW/substrate interface, and enables Fowler–Nordheim tunneling-dominated carrier transport. For self-driven photodetection, the NWs achieve a peak response at 520 nm (matching the core bandgap) with a responsivity of 0.8 mA/W, a detectivity of 6×10^7 Jones, and external quantum efficiency superior to most InGaN-based self-driven detectors. The PPC effect, originating from two types of DX centers (in core and shell) with electron redistribution, shows a bi-exponential decay ($\tau_1 = 0.42$ s and $\tau_2 = 3.78$ s) under 395 nm illumination. The SiN_x passivation ensures reproducible PPC decay and stable photodetection performance, confirming the NWs as a promising dual-functional platform for low-power optoelectronic applications.

I. INTRODUCTION

Memory and learning are fundamental for life development, while self-driven photodetection is increasingly critical for next-generation low-power optoelectronics. Many aspects of human memory—ultimately aiming to enhance learning and memory retention—are well understood, yet others remain difficult to access and design in psychological studies.[1] Simulating memory and learning properties is, therefore, essential, with computational methods widely used[2] and experimental simulators offering a complementary, ethically unrestricted approach. One prominent experimental platform leverages persistent photoconductivity (PPC) in semiconductors,[3–5] a phenomenon where photoconductivity (PC) decays rapidly initially after light illumination, followed by a slow long-term decay in the dark—attributed primarily to DX centers, stable doubly charged deep point defects that transition to singly charged metastable shallow donors via optical excitation.[6–8]

Basic human memory functions, such as paired-pulse facilitation (PPF) for short-term memory (STM) and the consolidation of STM into long-term memory (LTM), are readily reproduced by the PPC effect.[9] In these simulations, the product of illumination power and time corresponds to the total information received and retrieved, while PPC magnitude over time reflects memory buildup, loss, and forgetting. A decisive criterion for advanced memory simulators is reproducing the spacing effect[10–13]—the phenomenon where distributing learning and retrieval over time is more

effective for STM-to-LTM transition[14] than massed learning, up to an optimal spacing time. This effect arises from the delicate balance of learning, forgetting, and retrieval, as described by cognitive theories, including encoding variability, study-phase retrieval, and deficient-processing theories. Our preliminary work indicates that self-formed core–shell InGaN nanowires (NWs) can replicate the spacing effect via PPC, attributed to two types of DX centers (in core and shell) with distinct decay behaviors and electron redistribution.

Parallel to memory simulation, self-driven photodetection operating at 0 bias is highly sought after for low-power scenarios (e.g., Morse code decoding, field-deployed sensors) where external power sources are unavailable.[15,16] These devices rely on built-in electric fields to separate photogenerated carriers, demanding fast response dynamics (to distinguish signal pulses) and stable output (for accurate decoding).[17,18] However, existing materials rarely integrate PPC-based memory simulation and self-driven photodetection: traditional InGaN photodetectors excel at light detection but lack memory functionality, while PPC-based devices typically require external bias, increasing power consumption and limiting portability.[19,20]

InGaN NWs are ideal for integrating these functionalities due to their tunable bandgaps, strong quantum confinement, and low surface recombination.[21–23] Self-formed core–shell InGaN NWs—with an In-rich core (high In content and low bandgap) and In-poor shell (low In content and high bandgap)—further suppress surface recombination and stabilize DX centers via two-dimensional quantum confinement. In addition, SiN_x passivation layers can optimize interface properties by suppressing surface defects, stabilizing the NW/substrate contact, and enabling Fowler–Nordheim (F–N) tunneling for reliable carrier transport[24,25]—critical for both stable PPC decay and consistent photodetection performance.

Herein, we report SiN_x-passivated self-formed core–shell InGaN NWs that integrate dual functionalities: PPC for memory simulation and self-driven photodetection at 0 bias. We first revisit the origin of PPC[25–28] in these NWs (DX centers in core and shell) and confirm reproduction of basic memory functions[29,30] (PPF and STM-to-LTM transition). We then introduce the self-driven photodetection mechanism, enabled by band bending at the InGaN/SiN_x interface (similar to Schottky junction behavior). The SiN_x passivation layer plays a pivotal role in stabilizing both functionalities, ensuring reproducible PPC dynamics and robust photodetection. This dual-functional platform addresses unmet needs in low-power neuromorphic computing (memory simulation) and portable signal transmission (self-driven detection), opening avenues for integrated optoelectronic systems. The scheme of the dual-functional concept, core–shell NW structure, energy band diagram (DX centers and built-in electric field), and key results (spacing effect and photodetection response) are depicted in Fig. 1.

II. EXPERIMENTAL METHODS

The growth of the core–shell InGaN NWs was by PA-MBE on p-Si (111) substrates. Effusion cells for In and Ga supply and a radio frequency plasma source for active N supply were used. Before growth, the native oxide on the Si substrate surface was removed by etching for 2 min in 10 wt. % HF aqueous solution. Then, the cleaned Si substrate was loaded into the MBE buffer chamber and degassed in the MBE middle chamber for 1 h at 300 °C. The substrate was then transferred to the MBE growth chamber and first exposed to active N flux at 750 °C for nitridation, which improves the crystal quality. For the subsequent InGaN growth at 530 °C, calibrated by the onset of In desorption at 500 °C, the effusion cell temperatures for In and Ga were 710 and 820 °C, giving beam equivalent pressures of 2.6×10^{-7} and 7.3×10^{-7} Torr. The N plasma source settings were 390 W radio frequency (RF) power and 2.5 standard cubic centimeters per minute (sccm) molecular N_2 flow rate under slightly N-rich growth conditions. The growth rate was about 0.2 μm/h (planar, compact layer), and the growth time was 10 min. Basic characterization was by SEM, AFM, TEM, EDX, PL, and XRD.

60 nm Au was evaporated through a mask with 300×300 μm^2 area on top of the NWs, which forms a connected network for the electric top contact. GaIn eutectic was used for the electrical

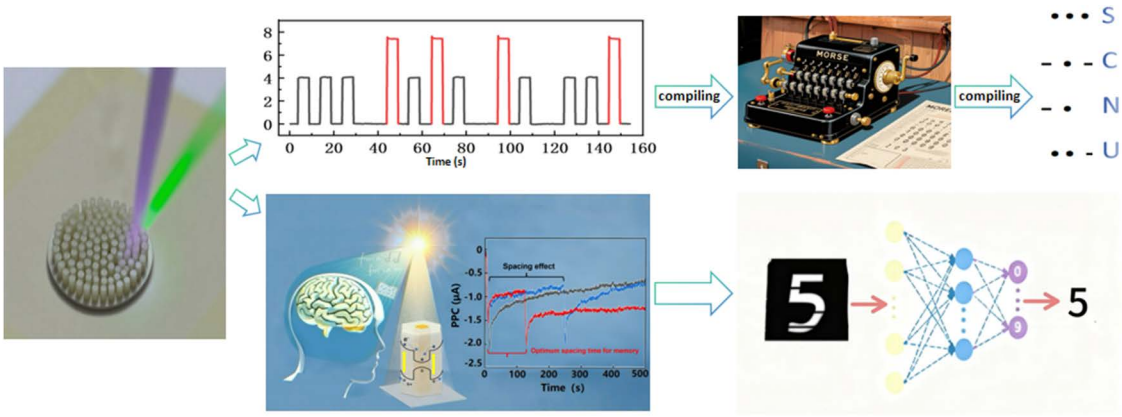

FIG. 1. Schematic illustration of the dual-functional SiN_x-passivated self-formed core–shell InGaN nanowire (NW) platform and its application scenarios: the left panel shows the core device structure (SiN_x-passivated core–shell InGaN NWs) under light excitation; the upper right panel shows that two light beams with distinct wavelengths irradiate the NW sample to activate the self-driven photodetection function (enabled by the built-in electric field at the InGaN/SiN_x interface), which is utilized for Morse code decoding (outputting "SCNU"); and the lower right panel shows that light excitation triggers the persistent photoconductivity (PPC) effect (originating from dual DX centers in the NW core and shell), whose dynamic decay behavior simulates neural network operations to realize the memory/learning functionalities demonstrated herein.

back contact. Diode lasers with emission wavelengths from the near-infrared (near-IR) to the ultraviolet (UV) were used for illumination. The power densities were adjusted using a calibrated Si photodetector. The applied voltage was 0.25 V, where the polarity is defined with respect to the back contact. The current was recorded using a Keithley 2400 source meter. To overwrite and reset any PPC effects between the experiments, a high-intensity light pulse was applied after each test, followed by a waiting period of approximately one hour. When the PPC approached again the same value under the same conditions for starting the preceding experiment, the successive experiment was started.

III. RESULTS AND DISCUSSION

The formation and the structural and optical properties of the self-formed core–shell InGaN NWs,[31,32] including applications for optical devices,[33,34] have been reported in detail and are recalled only briefly here. The NWs are grown by plasma-assisted molecular beam epitaxy (PA-MBE) on p-Si (111) substrates. InGaN NWs are usually formed on Si substrates for medium-to-low growth rates under slightly N-rich growth conditions. For growth temperatures above the onset of In desorption, a core–shell InGaN NW structure with an In-rich core and an In-poor shell naturally develops. This is based on the interplay of In supply, In surface diffusion, In desorption, and In incorporation on the NW sidewalls and NW top. Enhanced In desorption, on the NW sidewalls, leads to the In-rich core surrounded by the In-poor shell. In photoluminescence (PL) spectroscopy and x-ray diffraction (XRD) measurements, the PL spectra are dominated by the emission from the NW core and the XRD spectra are dominated by reflections from the NW shell. This is due to the transfer of photogenerated electrons and holes from the high-bandgap energy shell with low In content to the

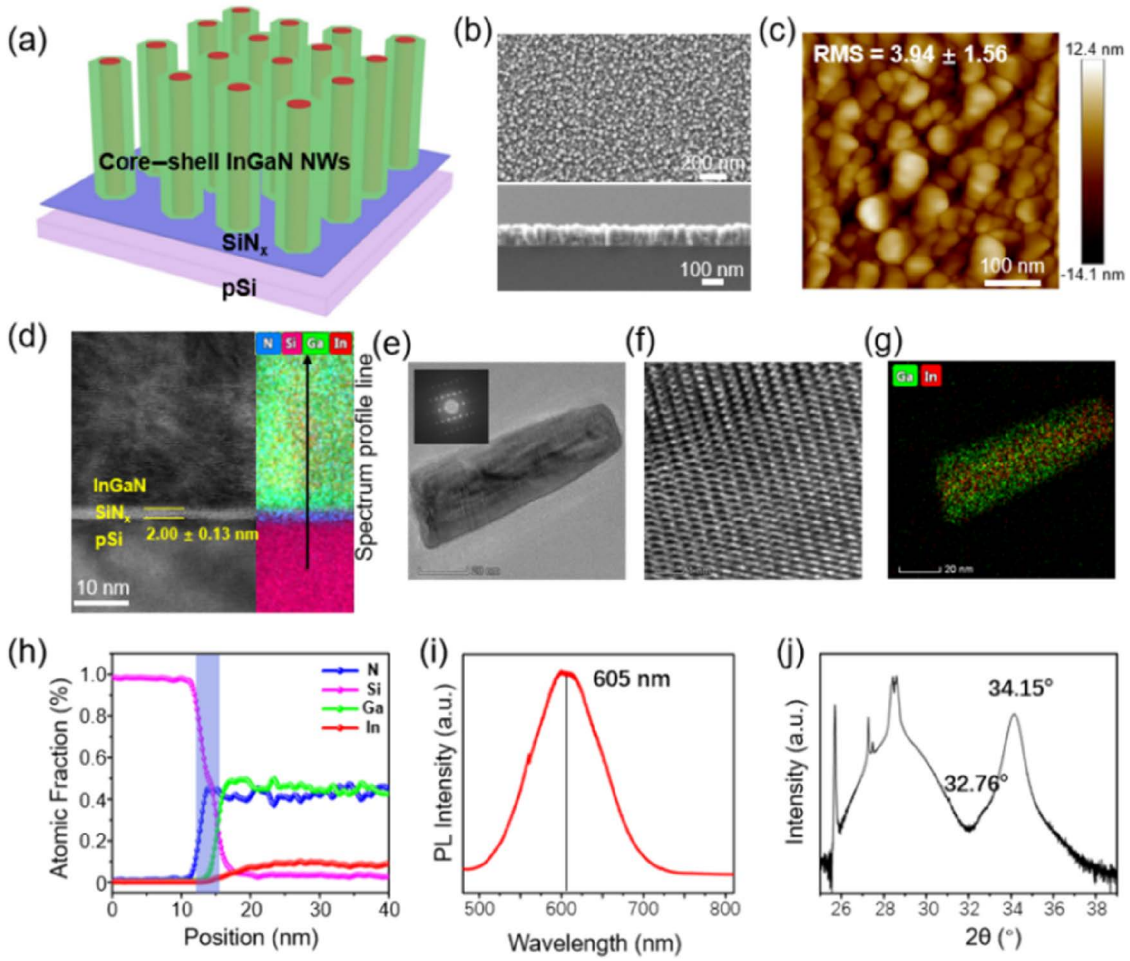

FIG. 2. Multi-characterization of core–shell InGaN nanowires (NWs) on p-Si substrates with a SiN_x layer: (a) schematic illustration; (b) top-view SEM image and cross-sectional SEM image of the InGaN NWs directly grown on the p-Si (111) substrate; (c) AFM image of the InGaN NWs. The root mean square (RMS) roughness is 3.94 ± 1.56 nm, likely limited by the AFM tip; (d) cross-sectional TEM image with atomic fraction profile (inset: EDX spectrum); (e) TEM image of a single core–shell InGaN NW with the electron diffraction image in the inset; (f) high-resolution TEM image of a single core–shell InGaN NW taken inside the orange square in (d); (g) EDX mappings of In and Ga of a single core–shell InGaN NW revealing the In-rich InGaN core surrounded by the In-poor InGaN shell; (h) atomic fraction profile along the NW radius; (i) room-temperature PL spectrum of the core–shell InGaN NWs; and (j) XRD spectrum of the core–shell InGaN NWs.

low-bandgap energy core with high In content regarding PL and the small core-to-shell volume ratio regarding XRD. Detailed characterization by scanning electron microscopy (SEM), atomic force microscopy (AFM), and transmission electron microscopy (TEM) together with energy dispersive x-ray (EDX) spectroscopy and mappings have directly imaged the core–shell structure with an around 10-nm-diameter InGaN core surrounded by a 10-nm-thick InGaN shell for the present NW sample. The NWs are straight and uniform with a length of ~110 nm. The deduced In contents and bandgap energies for the present NW sample are 55% and 2.05 eV (605 nm) for the core and 12% and 2.76 eV (450 nm) for the shell. The comparison of PL and XRD evidences strong two-dimensional lateral quantum confinement of electrons and holes in the NW core due to the small core diameter. The relevant SEM, AFM, TEM, EDX, PL, and XRD results are shown in Fig. 2.

To optimize the interface properties of core–shell InGaN NWs and clarify the carrier transport mechanism, we fabricated two sets of samples—with SiNx and without SiNx—and characterized their electrical transport properties via current–voltage (I–V) measurements and Fowler–Nordheim (F–N) tunneling fitting. The results are shown in Fig. 3, where panel (a) presents the I–V curves and panel (b) shows the F–N fitting curves.

The SiN_x-passivated sample exhibits distinct non-ohmic I–V behavior: under positive bias, the current increases slowly at low bias (<1 V) and shows a sharp jump at higher bias (>1 V), indicating a voltage-dependent carrier transport process; under negative bias, the current remains low and changes gently, reflecting asymmetric interface barrier characteristics. This voltage-dependent behavior (under external bias) is distinct from the 0-bias self-driven detection mechanism: for self-driven photodetection, the built-in electric field originates from band bending due to the core-shell InGaN NW/SiN_x interface [Fig. 3(c)]—a result of work function mismatch between InGaN (lower work function) and Si (higher work function), which forms a space charge region and drives photocarrier separation without external bias. Under external positive bias (top contact negative and bottom p-Si positive), the voltage-induced electric field across SiN_x (directed from top to bottom) overlaps with the built-in field, and their superposition determines carrier transport: at low bias (<2 V), the total electric field is insufficient to overcome the ~1.8 eV SiN_x potential barrier, so carriers are trapped at the InGaN/SiN_x interface; when bias exceeds 1 V, the enhanced total electric field enables electrons to tunnel through SiN_x via the F–N mechanism.

F–N tunneling is a typical carrier transport mechanism across dielectric barriers, described by the following formula:

$$J = \frac{q^3 E^2}{8\pi h \Phi} \exp\left(-\frac{8\pi\sqrt{2m^*\Phi^{3/2}}}{3qhE}\right), \tag{1}$$

where J is the current density, E is the electric field, m^* is the effective carrier mass, Φ is the barrier height, q is the electron charge, and h is Planck's constant. A linear relationship between $\ln\left(J/E^2\right)$ and $1/E$ indicates dominant F–N tunneling transport.

For the SiN_x-passivated sample, the F–N fitting curve under positive bias shows excellent linearity ($R^2 > 0.98$), confirming that F–N tunneling is the main carrier transport mechanism, where the SiN_x barrier provides a well-defined tunneling path. For the unpassivated sample, the F–N fitting curve is highly nonlinear. Therefore, all subsequent self-driven photodetection and PPC effect experiments

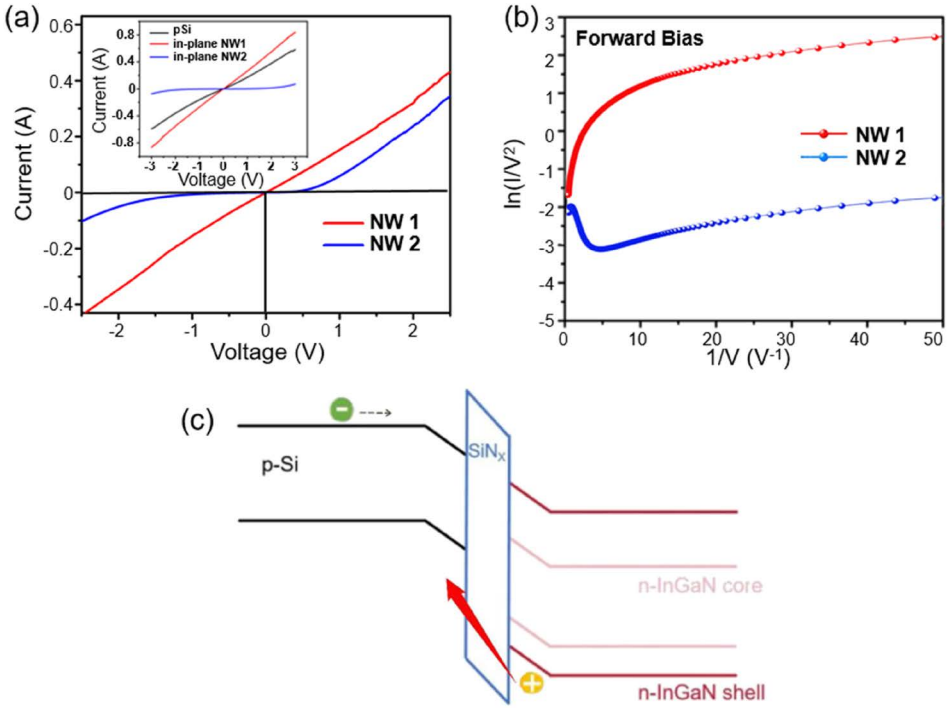

FIG. 3. (a) Current–voltage (I–V) characteristics of NW1 (unpassivated), NW2 (SiN_x-passivated), and p-Si substrate (inset); (b) $\ln(I/V^2)$ vs $1/V$ plots under forward bias for NW1 and NW2 (F–N tunneling fitting, showing the SiNx potential barrier of ~1.8 eV); (c) energy band diagram of p-Si/SiN_x/core-shell n-InGaN NW heterostructure.

were conducted on SiN_x-passivated samples to ensure consistent and reliable performance.

The InGaN NW/SiN_x interface enables efficient self-driven photodetection at 0 bias, where the internal built-in electric field is formed by band bending at the InGaN/SiN_x contact (similar to Schottky junction behavior)—this field separates photogenerated electron–hole pairs without external bias, while the SiN_x layer stabilizes the interface potential [Fig. 3(c)] to avoid defect-induced carrier recombination. The band bending originates from the work function difference between InGaN, SiN_x and Si forming a space charge region (depletion layer) in InGaN and Si; the resulting electric field (directed from InGaN to SiN_x) drives photogenerated electrons toward the InGaN NWs and holes toward the Si side, generating a net photocurrent. Notably, this detection system exhibits the strongest response at 520 nm—attributed to the optimal matching between 520 nm photon energy (2.38 eV) and the bandgap of the InGaN NWs (2.05 eV for the In-rich core), which maximizes photocarrier generation; the In-poor shell (12% In, 2.76 eV) primarily acts as a passivation layer for the core, reducing surface recombination rather than contributing to the built-in field.

Notably, this wavelength-dependent trend persists even at lower power densities (e.g., 3 mW/cm^2), where 520 nm still maintains the highest photocurrent density (5.2 μA/cm^2) compared to 4.1 μA/cm^2 at 450 nm, 1.1 μA/cm^2 at 405 nm, 4.1 μA/cm^2 at 650 nm,

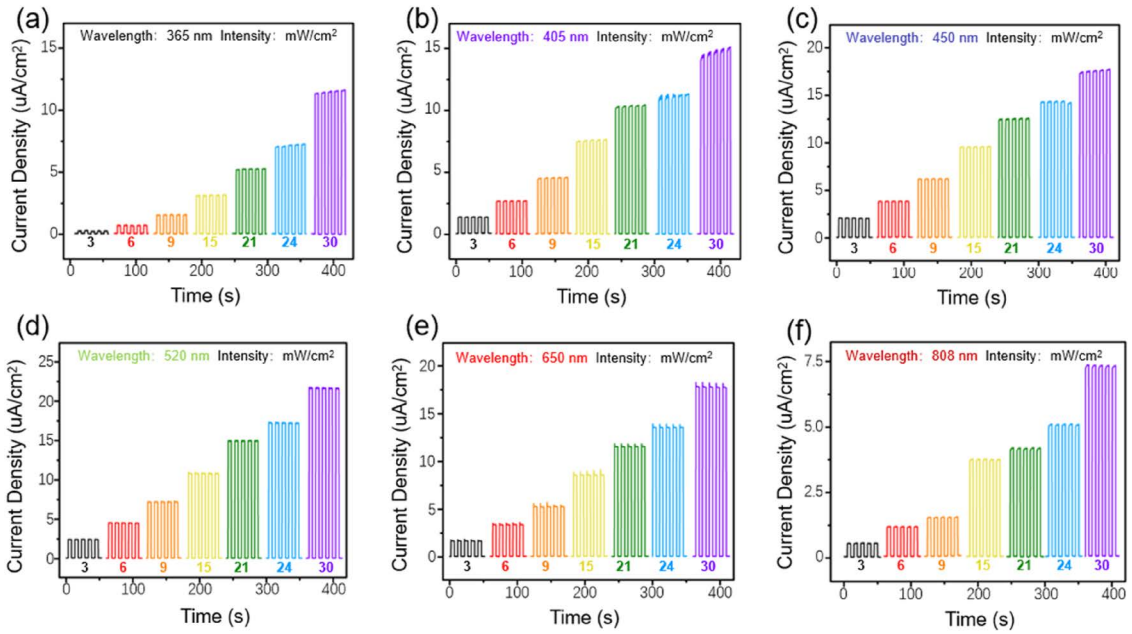

FIG. 4. [(a)–(f)] Photocurrent vs time characteristics of the photodetector at wavelengths of 365, 405, 450, 520, 650, and 808 nm, respectively, under incident power densities ranging from 3 to 30 mW/cm^2.

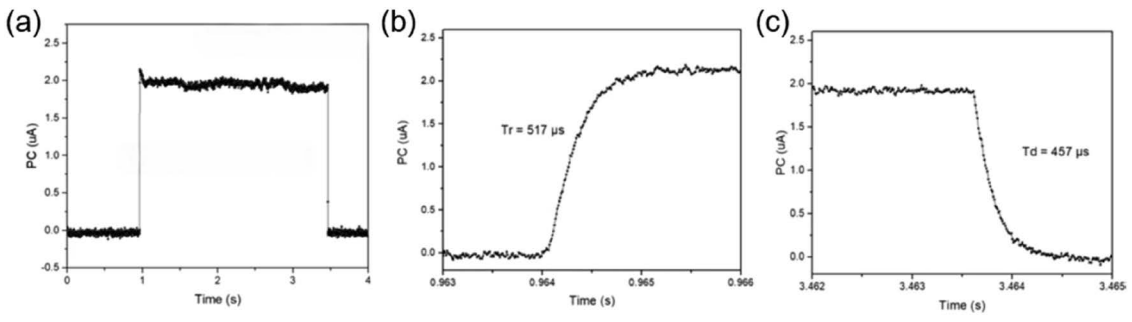

FIG. 5. (a) Photoresponse characteristics of the core–shell InGaN NWs under 520 nm illumination (30 mW/cm^2); time-dependent photocurrent curve under single light irradiation, enlarged view of the photocurrent (b) rising (τ_r = 517 μs) and (c) falling (τ_d = 457 μs) edges.

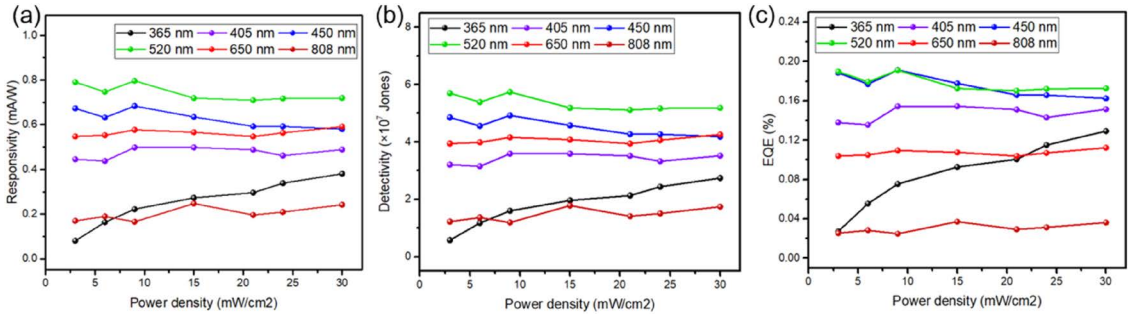

FIG. 6. (a) Responsivity, (b) detectivity, and (c) external quantum efficiency (EQE) of the photodetector as a function of power density at wavelengths of 365, 405, 450, 520, 650, and 808 nm.

and 3.0 μA/cm^2 at 808 nm (Fig. 4). This consistency confirms that the 520 nm peak response is not a power-dependent artifact but an intrinsic property of the core–shell structure, which is critical for practical applications such as Morse code decoding—where incident light intensity may fluctuate, but wavelength-specific response stability is required to reliably distinguish between "dot" (520 nm light) and "dash" (808 nm light) signals. The reproducibility of this trend across power densities also underscores the role of

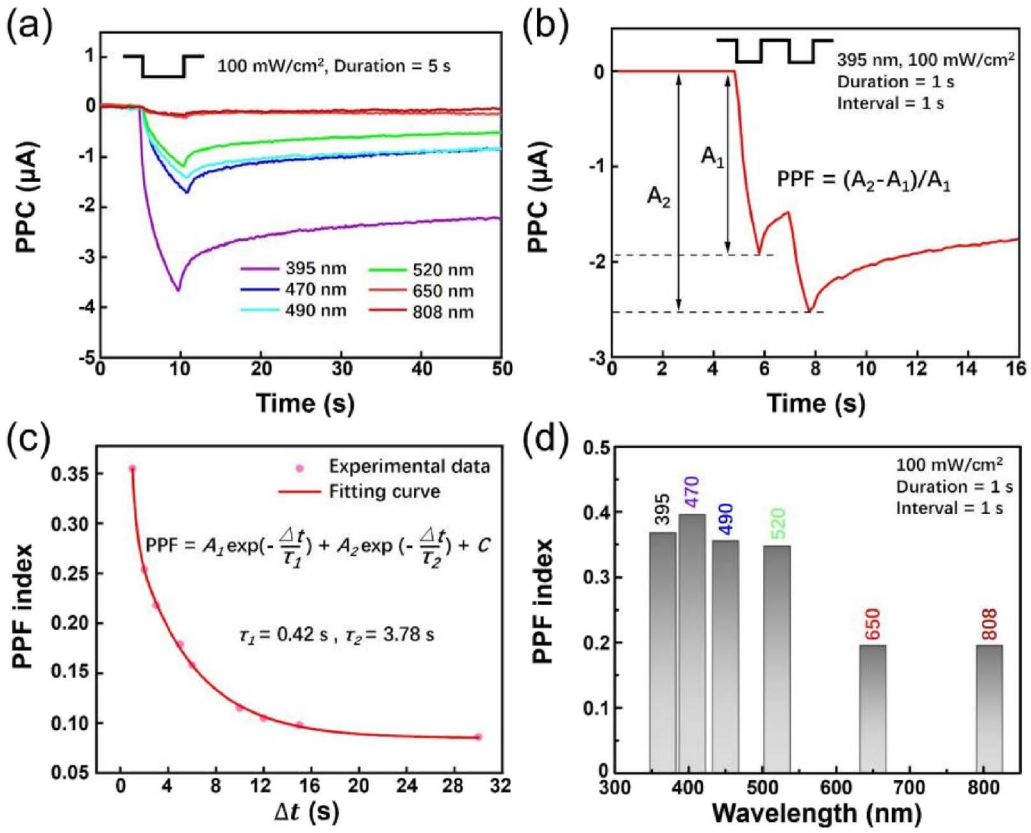

FIG. 7. (a) PC and PPC time traces for different light wavelengths, (b) PC and PPC time traces for two consecutive illumination pulses, (c) PPF index as a function of the time interval Δt between two pulses and fit by a bi-exponential function, and (d) PPF index for different light wavelengths.

SiN_x passivation in minimizing interface defect effects, ensuring that the core–shell NWs maintain consistent wavelength selectivity for self-driven photodetection.

To further characterize the fast response capability of the self-driven photodetector at the optimal wavelength (520 nm)—a key requirement for distinguishing "dot" and "dash" pulses in Morse code decoding—we measured the photoresponse under 30 mW/cm^2 illumination with high time resolution (Fig. 5). As shown in Fig. 5(a), the device exhibits a sharp, reproducible photocurrent peak upon light irradiation, with no obvious baseline drift (attributed to SiN_x passivation suppressing defect-induced carrier trapping). The transient dynamics [enlarged in Fig. 5(b)] reveal a fast rise time of 517 μs (defined as the time to reach 10%–90% of the maximum photocurrent) and a fall time of 457 μs (90%–10% of the maximum photocurrent). This response speed is superior to most reported InGaN-based self-driven photodetectors (typically millisecond-scale rise/fall times[6,7]), verifying the device's ability to capture rapid light signal changes without overlap.

To quantify the comprehensive performance of the core–shell InGaN NW photodetector, three key metrics—responsivity (R), detectivity (D*), and external quantum efficiency (EQE)—were calculated across different wavelengths and power densities (Fig. 6). All measurements were repeated three times, with error bars representing the standard deviation (n = 3), and the 520 nm wavelength exhibited the optimal performance across all metrics.

Responsivity (R), which reflects the device's photoelectric conversion efficiency, is defined as the ratio of the photocurrent density ($J_{ph} = I_{ph}/S$, where S = 0.1256 cm^2) to the incident light power density. As shown in Fig. 6(a), R first increases and then decreases with increasing wavelength, reaching a peak of 0.8 mA/W at 520 nm. This phenomenon arises from two factors: first, the photon energy of 520 nm (2.38 eV) matches the bandgap of the In-rich core (2.05 eV), enabling efficient absorption by the core without absorption competition with the In-poor shell (bandgap = 2.76 eV, which only absorbs light with $\lambda < 450$ nm); second, carriers excited by bandgap-matched photons have higher mobility with reduced interface scattering loss.

Detectivity (D*), a critical metric for evaluating a device's weak-light detection capability, is calculated using the formula $D^* = R/\sqrt{(2qJ_{dark})}$, where $q = 1.6 \times 10^{-19}$ C (electron charge) and $J_{dark} = 4.8 \times 10^{-8}$ A/cm^2 (dark current density). As shown in Fig. 6(b), D* follows the same variation trend as the responsivity, achieving a maximum value of 6×10^7 Jones at 520 nm—confirming that 520 nm is the optimal wavelength for the device in

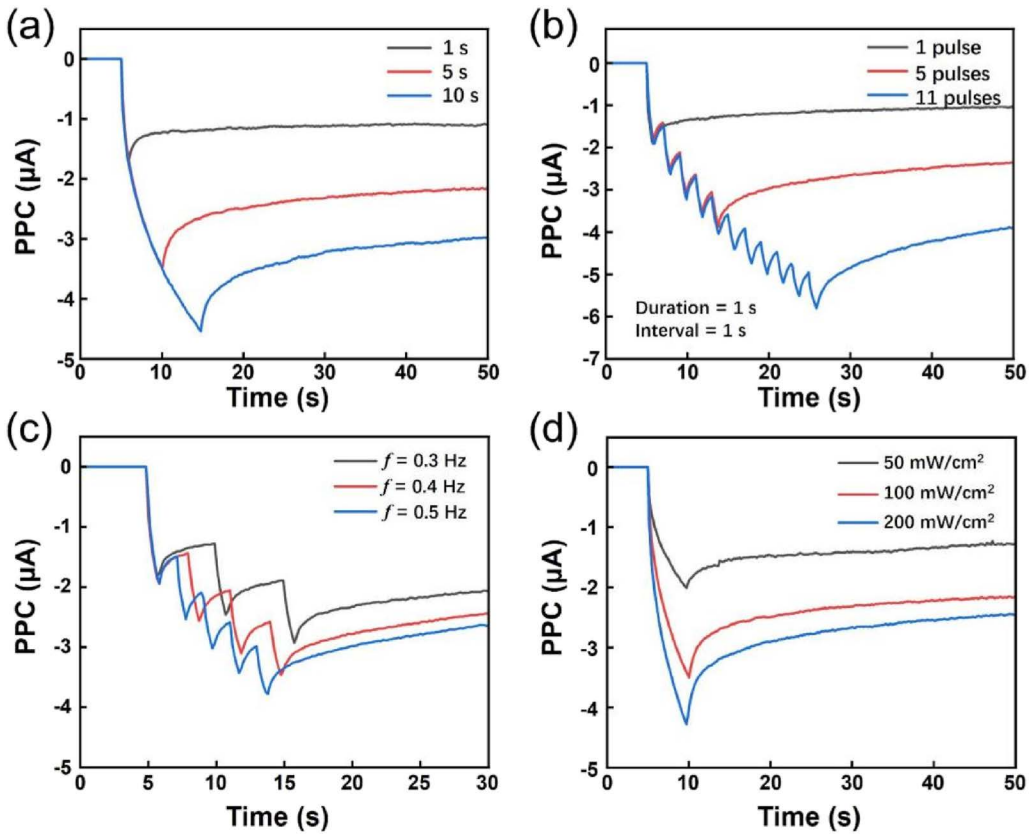

FIG. 8. PC and PPC time traces for (a) increasing illumination time under continuous illumination, (b) increasing illumination time under pulsed illumination, (c) pulsed excitation with increasing frequency, and (d) increasing illumination power density under continuous illumination.

weak-light detection scenarios (e.g., low-illumination environmental monitoring).

External quantum efficiency (EQE) describes the efficiency of photon-to-carrier conversion and is calculated using the formula EQE = 1240R/λ (where hc = 1240 eV·nm, λ is the wavelength, and R is the responsivity). As shown in Fig. 6(c), the EQE performance of the device is superior to that of most InGaN-based self-driven photodetectors in the visible–near-infrared crossover band, laying a foundation for the device's application in dual-mode (visible–near-infrared) imaging.

To simulate the STM response, Fig. 7(b) shows a typical PPF experiment. Two consecutive light pulses are applied, which are separated in time by the relatively short interval Δt. The illumination pulse duration is 1 s, the power density is 100 mW/cm^2, and the wavelength is 395 nm. The ratio of the two PC peaks (A2-A1)/A1, which is the PPF index, is plotted in Fig. 7(c) as a function of Δt. Due to the relatively fast initial PPC decay or STM loss, the PPF index strongly decreases with Δt but levels off when the decay becomes slower for longer time intervals, approaching the transition to the LTM. The PPF index decreases in magnitude from 0.35 to 0.10 within 30 s. This is fitted by a bi-exponential function of the form

$$\text{PPF index} = A_1 \exp\left(-\Delta t/\tau_1\right) + A_2 \exp\left(-\Delta t/\tau_2\right) + C. \quad (2)$$

Here, A_1 and A_2 are the initial PC values, C is a constant, and τ_1 and τ_2 are the fast and slow decay time constants of 0.42 and 3.78 s. Figure 7(d) shows the PPF index measured for different wavelengths. When only the DX centers in the NW core are excited for 808 and 650 nm, the PPF index is small. It drastically increases when also the DX centers in the shell are excited for 520 nm and stays relatively constant for the shorter wavelengths. This is the final confirmation of the two types of DX centers in the NW core and shell and, regarding the overall PC and PPC response, justifies that all experiments to simulate the human memory are carried out with 395 nm light wavelength.

The transfer from STM to LTM for longer times and/or higher learning and retrieval intensity is illustrated by the PC and PPC buildup and decay time dependencies in Figs. 8(a)–8(d) for (a) increasing illumination time under continuous illumination, (b) increasing illumination time under pulsed illumination, (c) pulsed excitation with increasing frequency, and (d) increasing illumination power density under continuous illumination. The illumination power density in (a)–(c) is 100–0.25–0.25 V. The wavelength is 395 nm in (a)–(d). The pulse durations, the number of repetitions, frequencies, and excitation power densities are indicated. The built-up of the LTM is reflected by the increasing PPC after longer illumination times with continuous or repeated or stronger illumination pulses. Continuous or pulsed illumination with different illumination powers mimics the retrieval practice with different lengths, frequencies, numbers, and effectivenesses after the initial learning event.

IV. CONCLUSIONS

Self-formed core–shell InGaN NWs passivated with a SiN_x layer integrate two critical optoelectronic functionalities, tailored for target applications in Morse code decoding and artificial neural networks. For 0-bias self-driven photodetection, the NWs exhibit optimized performance at a 520 nm-responsivity of 0.8 mA/W, a detectivity of 6×10^7 Jones, and fast transient dynamics (rise time ~0.517 ms and fall time ~0.457 ms)—enabling accurate decoding of light-based Morse code signals without external power, addressing the demand for portable, low-power communication systems. For bias-dependent PPC, the dual DX center system (core + shell) enables tunable STM-to-LTM transition: single light stimulation induces fast-decaying STM (τ_1 = 0.42 s, weak synaptic weight), while dual light stimulation induces slow-decaying LTM (τ_2 = 3.78 s, strong synaptic weight)—mimicking synaptic plasticity essential for neural network learning.

The SiN_x passivation layer plays a critical role in stabilizing both functionalities: it suppresses interface defects to enhance photodetection stability and enables F–N tunneling for reliable carrier transport in PPC. The core–shell structure, with its In-rich core and In-poor shell, further optimizes performance by leveraging quantum confinement to stabilize deep DX centers and suppressing surface recombination of the core; the built-in electric field driving self-driven photocarrier separation originates from band bending at the InGaN/SiN_x/Si interfaces. This work establishes core–shell InGaN NWs as a versatile platform that bridges low-power signal transmission and neuromorphic memory, advancing the development of integrated optoelectronic devices for next-generation communication and computing systems.

ACKNOWLEDGMENTS

This work was supported by the Program for Changjiang Scholars and Innovative Research Team in University (Grant No. IRT_17R40), MOE International Laboratory for Optical Information Technologies, and the 111 Project.

AUTHOR DECLARATIONS

Conflict of Interest

The authors have no conflicts to disclose.

Author Contributions

R. Deng, B. Lin, and X. Pu performed the growth under supervision of R. Nötzel. J. Li performed the experiments. R. Nötzel supervised the research and drafted the manuscript together with J. Li.

Junyong Li: Conceptualization (lead); Data curation (lead); Investigation (lead); Writing – original draft (equal). **Rongli Deng**: Conceptualization (lead); Data curation (lead); Investigation (lead); Writing – review & editing (equal). **Haibin Lin**: Writing – review & editing (supporting). **Xuan Pu**: Conceptualization (supporting). **Richard Nötzel**: Conceptualization (equal); Resources (lead); Supervision (lead); Writing – original draft (lead); Writing – review & editing (equal).

DATA AVAILABILITY

The data that support the findings of this study are available from the corresponding author upon reasonable request.

REFERENCES

[1] Z. Ye, B. Zhang, V. Nguyen, Y. Pan, K. Li, and Z. Mi, "Self-templated sputtering synthesis of III-nitride nanowire array for solar water splitting," Nano Lett. **25**(42), 15305–15312 (2025).

[2] Z. Liu, J. Li, F. Wang, W. Wang, Z. Li, J. You, Z. Chen, Y. Li, X. Wang, and J. Ao, "Investigation of high-temperature diamond UV photodetectors with MSM and SBD structure fabricated by selectively grown method," IEEE Sens. J. **25**(16), 30642–30648 (2025).

[3] T. Su, B. Xiao, Z. Ai, L. Bao, W. Chen, Y. Shen, Q. Cheng, and K. Ken Ostrikov, "High-rate growth of gallium oxide films by plasma-enhanced thermal oxidation for solar-blind photodetectors," Appl. Surf. Sci. **624**, 157162 (2023).

[4] J. Zhang, B. Jiao, J. Dai, D. Wu, Z. Wu, L. Bian, Y. Zhao, W. Yang, M. Jiang, and S. Lu, "Enhance the responsivity and response speed of self-powered ultraviolet photodetector by GaN/$CsPbBr_3$ core-shell nanowire heterojunction and hydrogel," Nano Energy **100**, 107437 (2022).

[5] J. B. Bokka and B. V. J. Doddi, "Line-tunneling based GaP/Si heterostructure vertical gate-all-around tunnel FET for enhanced electrical performance," Mater. Sci. Eng.: B **312**, 117875 (2025).

[6] Z. Yang, B. Lin, L. Wang, J. Du, and S. Sun, "Self-driven PbI_2-based ultraviolet photodetectors with ultrafast response," ACS Appl. Electron. Mater. **7**(9), 4125–4132 (2025).

[7] F. Meng, Z. Xu, Y. Zeng, C. Wang, Y. Zou, S. Wageh, A. A. Al-Ghamdi, Z. Guo, and H. Zhang, "Photodetectors based on MoS_2/$MAPbBr_3$ van der Waals heterojunction," IEEE Electron Device Lett. **43**(3), 414–417 (2022).

[8] X. Tian and Y. Liu, "Van der Waals heterojunction $ReSe_2$/WSe_2 polarization-resolved photodetector," J. Semicond. **42**(3), 032001 (2021).

[9] Z. Wang, M. Wang, H. Nan, J. Bai, and C. Wang, "Effect of thickness on optical properties of InSe/In_2Se_3 heterojunction," AIP Adv. **14**(8), 085225 (2024).

[10] Editorial, "Focus on learning and memory," Nat. Neurosci. **22**(10), 1535 (2019).

[11] A. G. E. Collins and A. Shenhav, "Advances in modeling learning and decision-making in neuroscience," Neuropsychopharmacology **47**(1), 104–118 (2022).

[12] A. Paul, N. Sajid, L. Da Costa, and A. Razi, "On efficient computation in active inference," Expert Syst. Appl. **253**, 124315 (2024).

[13] A. Sumanth, K. Lakshmi Ganapathi, M. S. Ramachandra Rao, and T. Dixit, "A review on realizing the modern optoelectronic applications through persistent photoconductivity," J. Phys. D: Appl. Phys. **55**(39), 393001 (2022).

[14] S.-L. Gao, L.-P. Qiu, J. Zhang, W.-P. Han, S. Ramakrishna, and Y.-Z. Long, "Persistent photoconductivity of metal oxide semiconductors," ACS Appl. Electron. Mater. **6**(3), 1542–1561 (2024).

[15] C. G. Van de Walle, "Stretched-exponential relaxation modeled without invoking statistical distributions," Phys. Rev. B **53**(17), 11292–11295 (1996).

[16] R. Nossek, "Ein experimenteller Beitrag zur Theorie des elektrischen Widerstandes der Metalle," Z. Naturforsch. A **16**(11), 1162–1172 (1961).

[17] B. Sturman, E. Podivilov, and M. Gorkunov, "Origin of stretched exponential relaxation for hopping-transport models," Phys. Rev. Lett. **91**(17), 176602 (2003).

[18] A. S. Benjamin and J. Tullis, "What makes distributed practice effective?," Cognit. Psychol. **61**(3), 228–247 (2010).

[19] S. K. Carpenter, N. J. Cepeda, D. Rohrer, S. H. K. Kang, and H. Pashler, "Using spacing to enhance diverse forms of learning: Review of recent research and implications for instruction," Educ. Psychol. Rev. **24**(3), 369–378 (2012).

[20] E. Gerbier and T. C. Toppino, "The effect of distributed practice: Neuroscience, cognition, and education," Trends Neurosci. Educ. **4**(3), 49–59 (2015).

[21] P. Smolen, Y. Zhang, and J. H. Byrne, "The right time to learn: Mechanisms and optimization of spaced learning," Nat. Rev. Neurosci. **17**(2), 77–88 (2016).

[22] S. K. Carpenter, S. C. Pan, and A. C. Butler, "The science of effective learning with spacing and retrieval practice," Nat. Rev. Psychol. **1**(9), 496–511 (2022).

[23] R. Deng, X. Pan, H. Lin, J. Li, and R. Nötzel, "Evidence of two-dimensional lateral quantum confinement in self-formed core–shell InGaN nanowires on Si (111) emitting in the red," Appl. Phys. Lett. **124**(22), 222102 (2024).

[24] A. Citri and R. C. Malenka, "Synaptic plasticity: Multiple forms, functions, and mechanisms," Neuropsychopharmacology **33**(1), 18–41 (2008).

[25] G. Beadie, W. S. Rabinovich, A. E. Wickenden, D. D. Koleske, S. C. Binari, and J. A. Freitas, Jr., "Persistent photoconductivity in n-type GaN," Appl. Phys. Lett. **71**(8), 1092–1094 (1997).

[26] C. H. Qiu and J. I. Pankove, "Deep levels and persistent photoconductivity in GaN thin films," Appl. Phys. Lett. **70**(15), 1983–1985 (1997).

[27] C. V. Reddy, K. Balakrishnan, H. Okumura, and S. Yoshida, "The origin of persistent photoconductivity and its relationship with yellow luminescence in molecular beam epitaxy grown undoped GaN," Appl. Phys. Lett. **73**(2), 244–246 (1998).

[28] P. B. Klein, J. A. Freitas, Jr., S. C. Binari, and A. E. Wickenden, "Observation of deep traps responsible for current collapse in GaN metal–semiconductor field-effect transistors," Appl. Phys. Lett. **75**(25), 4016–4018 (1999).

[29] M. Zhou, Y. Zhao, X. Gu, Q. Zhang, J. Zhang, M. Jiang, and S. Lu, "Realize low-power artificial photonic synapse based on (Al,Ga)N nanowire/graphene heterojunction for neuromorphic computing," APL Photonics **8**(7), 076107 (2023).

[30] M. Zhou, Y. Zhao, X. Gu, Q. Zhang, J. Zhang, M. Jiang, and S. Lu, "Light-stimulated low-power artificial synapse based on a single GaN nanowire for neuromorphic computing," Photonics Res. **11**(10), 1667–1677 (2023).

[31] X. Pan, H. Hong, R. Deng, M. Luo, and R. Nötzel, "In desorption in InGaN nanowire growth on Si generates a unique light emitter: From in-rich InGaN to the intermediate core–shell InGaN to pure GaN," Cryst. Growth Des. **23**(8), 6130–6135 (2023).

[32] R. Deng, X. Pu, G. Yang, W. Zhang, H. Lin, J. Li, and R. Nötzel, "Temperature and source flux dependence of light emission, in incorporation and quantum confinement in self-formed core–shell InGaN nanowires," Cryst. Growth Des. **24**(18), 7653–7661 (2024).

[33] X. Pan, J. Song, H. Hong, M. Luo, and R. Nötzel, "Red InGaN nanowire LED with bulk active region directly grown on p-Si (111)," Opt. Express **31**(10), 15772–15778 (2023).

[34] X. Pan, R. Deng, H. Hong, M. Luo, and R. Nötzel, "Sign reversal of visible to UV photocurrent in core–shell n-InGaN/p-GaN nanowire photodetectors," J. Appl. Phys. **136**(3), 034501 (2024).